Two serial filters control P2X7 cation selectivity, Ser342 in the central pore and lateral acidic residues at the cytoplasmic interface

Fritz Markwardt [a,*,1], Eike Christian Schön [a,1], Michaela Raycheva[b], Aparna Malisetty[b,2], Sanaria Hawro Yakoob[b], Malte Berthold[a] and Günther Schmalzing [b,*]

[a]Julius-Bernstein-Institute of Physiology, Martin-Luther-University, Magdeburger Straße 6, D-06097 Halle/Saale, Germany
[b]Institute of Clinical Pharmacology, RWTH Aachen University, Wendlingweg 2, D-52074 Aachen, Germany
*To whom correspondence should be addressed: Email: fritz.markwardt@medizin.uni-halle.de (F.M.); Email: gschmalzing@ukaachen.de (G.S.)
[1]F.M. and E.C.S. contributed equally to this work.
[2]Present address: Hybrid Materials Interfaces Group, Faculty of Production Engineering, University of Bremen, Bremen, Germany
Edited By Ivet Bahar

Abstract

The human P2X7 receptor (hP2X7R) is a homotrimeric cell surface receptor gated by extracellular ATP^{4-} with two transmembrane helices per subunit, TM1 and TM2. A ring of three S342 residues, one from each pore-forming TM2 helix, located halfway across the membrane bilayer, functions to close and open the gate in the apo and ATP^{4-}-bound open states, respectively. The hP2X7R is selective for small inorganic cations, but can also conduct larger organic cations such as $Tris^+$. Here, we show by voltage-clamp electrophysiology in *Xenopus laevis* oocytes that mutation of S342 residues to positively charged lysines decreases the selectivity for Na^+ over $Tris^+$, but maintains cation selectivity. Deep in the membrane, laterally below the S342 ring are nine acidic residues arranged as an isosceles triangle consisting of residues E14, D352, and D356 on each side, which do not move significantly during gating. When the E14K mutation is combined with lysine substitutions of D352 and/or D356, cation selectivity is lost and permeation of the small anion Cl^- is allowed. Lysine substitutions of S342 together with D352 or E14 plus D356 in the acidic triangle convert the hP2X7R mutant to a fully Cl^--selective ATP^{4-}-gated receptor. We conclude that the ion selectivity of wild-type hP2X7R is determined by two sequential filters in one single pathway: (i) a primary size filter, S342, in the membrane center and (ii) three cation filters lateral to the channel axis, one per subunit interface, consisting of a total of nine acidic residues at the cytoplasmic interface.

Significance Statement

Pore size and electrostatic interactions are key to the permeation selectivity of ion channels. Previous cysteine scanning mutagenesis identified a tri-serine-342 ring located halfway across the membrane as the gate and selectivity filter of the P2X7 receptor (P2X7R) channel, accessible from the inside to cationic but not anionic reagents. Consistent with a downstream cation filter, we could now switch P2X7R from cation to anion selectivity by lysine substitution of acidic residues at the cytoplasmic interface. Our data show that two sequential selectivity filters control the cation selectivity of the P2X7R channel, a dynamic tri-serine-342 size filter and three conformationally static cation filters of three acidic residues each. We propose that the ion selectivity of P2X receptors involves the mechanism described here.

Introduction

The P2X7 receptor (P2X7R) is an ATP^{4-}-gated cation-selective channel that is of great interest as a drug target (1) because of its widespread expression in virtually all immune cells, including microglia (2) and also tumor cells (3), its role in inflammation, and also because of its enigmatic ability to generate large cytotoxic pores (4). Extracellular binding of the ligand ATP^{4-} opens the channel pore within milliseconds to small cations such as Na^+, K^+, and Ca^{2+}, but also allows permeation of larger organic cations, including $Tris^+$ (121 Da), N-methyl-D-glucamine$^+$ (NMDG$^+$, 195 Da) and cationic DNA-binding dyes such as ethidium$^+$ (314 Da) and Yo-Pro-1^{2+} (376 Da).

For many years, the permeation of large cations was attributed to a second conducting state in which the P2X7R channel pore gradually increases upon continued stimulation with ATP (5), eventually leading to membrane blebbing and cytolysis (6, 7). In contrast to whole-cell recordings, single-channel recordings of ATP^{4-}-induced currents in human P2X7R (hP2X7R)-expressing human B lymphocytes (8) and *Xenopus laevis* oocytes provided no evidence for a time-dependent increase in pore diameter (9). Instead, single-channel recordings showed a low instantaneous permeability to $Tris^+$ (mean diameter 5.8 Å, for ionic diameter references, see Table 1), NMDG$^+$ (mean diameter 7.3 Å), and other large cations, which remained constant until ATP^{4-} was washed out (10). This view is supported

Table 1. Compilation of ion diameter (in Å).

Anorganic[a]	Dehydrated	Ref.	Hydrated	Ref.	Hydration number	Ref.
$^{VI}Cl^-$	3.62^{IR}	(11)	6.64	(12)	~6	(13)
$^{VI}K^+$ "Pauling"	2.66	(14)				
$^{VI}K^+$	2.74^{IR}	(11)	6.62	(12)	~6	(15)
Na^+ "Pauling"	1.90	(14)				
$^{V}Na^+$	2.00^{IR}, 2.04	(11, 16)	7.16	(12)	~5	(13, 15)

Organic	Dimensions	Mean diameter[b]	Ref.
Glu^-	5.5×6.5		(17)
$MTSES^-$	$5.8 \times 5.8 \times 10$		(18)
$MTSEA^+$	$4.6 \times 4.6 \times 10$		(18)
$MTSET^+$	$5.8 \times 5.8 \times 10$		(18)
$NMDG^+$	$5.0 \times 6.4 \times 12.0$	7.3	(19)
$NMDG^+$	$6.5 \times 8.7 \times 10.8$	8.4	(20)
$Tris^+$	$6.0 \times 6.9 \times 7.7$	6.8	(21)
$Tris^+$	$5.5 \times 5.6 \times 6.4$	5.8	(19)
$Tris^+$	$6.4 \times 6.5 \times 7.5$	6.8	(20)
Yo-Pro-1^{2+}	$8.2 \times 12.8 \times 16.8$	12.0	(20)
Zwitterion			
HEPES		~10	(22)

[a]Roman superscripts V and VI denote the oxidation states; superscript IR denotes effective radius as stated in the respective references.
[b]Mean diameter was calculated as the geometric mean of the dimensions of a box containing the ion, as previously proposed (19).

and extended by data showing instantaneous robust NMDG$^+$ currents in HEK293 cells with the P2X2 receptor (23) and all homotrimeric P2X receptors except P2X1 (24). Also, the purified liposomal reconstituted panda P2X7R (pdP2X7R), which shares 85% sequence identity with hP2X7R, has been shown to be intrinsically permeable to the cationic dye YO-PRO-1 (376 Da, mean diameter 12 Å) (25).

Plotting the single-channel conductance against the apparent molecular diameter of the permeating organic cations yielded an ATP^{4-}-opened effective pore diameter of ~8.5 Å of the hP2X7R, which was stable over time (10). Considering the different measurement methods [single-channel recordings versus cryo-electron microscopy (cryo-EM)] and species (human versus rat), the open pore diameter of ~8.5 Å in *X. laevis* oocytes is in reasonable agreement with the structural diameter of 5.0 Å at S342 of rP2X7R reconstituted in detergent micelles (26). The apo-closed cryo-EM structure of rP2X7R shows that the pore is completely collapsed between residues S339 and S342, which define the extracellular and intracellular boundaries of the TM2 gate, respectively (26). This is consistent with cysteine scanning accessibility mutagenesis, which showed that the closed channel is accessible from the outside up to residue S339, but not up to S342 (27).

A tri-serine ring with a pore diameter of 5.0 Å and larger, which might allow even fully hydrated Na$^+$ or K$^+$ with diameters of ~5 (28) or ~6 Å (18) to pass, is difficult to reconcile with the selective discrimination of small cations. We therefore asked here whether the hP2X7R possesses acidic residues that discriminate between anions and cations by repulsion and attraction. An exception to the strict cation permeability of other members of the P2XR family is the P2X5R, which exhibits significant anion permeability in addition to cation permeability (29, 30). Recently, a basic residue in P2X5 receptors that replaces glutamate in the cytoplasmic lateral fenestrations of purely cation-selective P2XRs was shown to be responsible for anion permeability (31). To investigate which residues in the transmembrane pathway of hP2X7R control the size and charge of permeant cations, we electrophysiologically characterized lysine mutants of S342 and downstream acidic residues at the plasma membrane–cytoplasmic interface and used homology models based on the apo-closed and open cryo-EM structure of rP2X7R (26) for interpretation. We found that cationic selectivity is determined by two serial filters in a single pathway, a primary size-screening filter midway in the membrane formed by a ring of three S342 residues, one per subunit, and a primary electrostatic filter further downstream and lateral to S342 formed by a total of 9 acidic residues, 3 per subunit, located in the membrane–cytoplasmic interface.

Materials and methods
Reagents
Unless otherwise stated, standard chemicals were purchased from Merck/Sigma Aldrich (Darmstadt, Germany). Na$_2$ATP was purchased from Roche (Mannheim, Germany). Molecular biology reagents were purchased from New England Biolabs (Schwalbach, Germany) with the exception of the antireverse cap analog m7,3′-OGpppG (product NU-855), which was purchased from Jena Bioscience, Germany.

Homology modeling of the hP2X7 homotrimer and point mutants in the apo-closed and open states
According to a ClustalW alignment (32), the primary sequence identity between hP2X7 (Q99572) and rP2X7 (Q64663) is 80.3%. Using Swiss-Modeler (https://swissmodel.expasy.org) and the cryo-EM structures of rat P2X7R (rP2X7R) in the apo-closed state (PDB 6U9V) and in the ATP-bound open state (PDB 6U9W) as templates (26), we generated homology models of hP2X7R^{wt} and mutants and visualized them using PyMOL (Schrödinger LLC. The PyMOL molecular graphics system, version 1.3r1. Portland. 2010 Oregon: Schrödinger, LLC.). To calculate pores and tunnels in the homology-modeled hP2X7R structures, we used MOLEonline (33) and visualized them using the built-in LiteMole viewer or after downloading the results in PyMOL format using PyMOL software.

Generation of hP2X7R mutants
The plasmid encoding the wt hP2X7R subunit (P2RX7_HUMAN, UniProtKB Q99572) in our oocyte expression vector pNKS2 (34) was the same as in our previous studies (9, 10, 27, 35). Point mutants were designed using Vector NTI software (InforMax v. 4.0)

and generated using the QuickChange method for site-directed mutagenesis (36). The primers used are listed in SI Appendix, Table S2. Mutants were screened by restriction pattern analysis and verified by commercial DNA sequencing (MWG, Ebersberg, Germany) and sequence alignment. Capped and polyadenylated cRNAs were synthesized from XhoI-linearized DNA templates as described previously (37).

Expression of hP2X7R^{wt} and its mutants in *X. laevis* oocytes

The maintenance of the frogs and the surgical removal of parts of their ovaries were approved by the local animal care committee (ref no. 42502-2-1493 MLU) according to the EC Directive 86/609/EEC for animal experiments. After defolliculation with collagenase NB 4G (Nordmark Pharma GmbH, Uetersen, Germany), Dumont stage V and VI oocytes were injected with 46 nl of cRNA containing 1 ng or 50 ng of wt or mutant hP2X7R, respectively. Injected oocytes were maintained at 19°C in oocyte Ringer's solution [ORi: 100 mM NaCl, 1 mM KCl, 1 mM MgCl$_2$, 1 mM CaCl$_2$, 10 mM N-[2-hydroxyethyl]piperazine-N′-[2-ethanesulfonic acid] (HEPES)–NaOH, pH 7.4] supplemented with penicillin (100 U/ml) and streptomycin (100 μg/ml) until used 1–3 days later.

Quantification of cell surface expression of hP2X7R constructs in *X. laevis* oocytes

hP2X7 proteins were labeled with IR800 NHS ester (Li-COR) on the surface of intact oocytes, extracted with digitonin, purified through their C-terminal double-strepII tag using Strep-Tactin Sepharose (IBA Lifesciences), resolved by SDS–PAGE, and detected as IR800 fluorescence on the wet PAGE gel using a LI-COR Odyssey scanner (27, 38, 39). hP2X7R IR800 fluorescence was quantified using Image Lab software (Bio-Rad).

Two-electrode voltage-clamp recordings from *X. laevis* oocytes

Currents were recorded at room temperature (~22°C) using an OC-725C oocyte clamp amplifier (Warner Instruments, Hamden, USA), filtered at 100 Hz, and sampled at 500 Hz as previously described (30, 37, 40). The reference electrodes were connected to the bath via 3 M KCl agar bridges. The remaining diffusion potentials were measured according to a previously published method (41). In the Tris$^+$-Glu$^-$-based extracellular solution, this potential was −8 mV and was corrected accordingly. The diffusion potential for Cl$^-$-based bath solutions was negligibly small (<0.5 mV).

While superfused with ORi, individual oocytes were impaled with 3 M KCl-filled glass microelectrodes with resistances of 1.2–1.4 MΩ. hP2X7R-dependent currents were measured in nominally Ca^{2+}- and Mg^{2+}-free bath solutions consisting of either 100 mM NaCl, 100 mM TrisCl, or 100 mM Tris–glutamate supplemented with 0.1 mM flufenamic acid, 1 mM ethylene glycol tetraacetic acid (EGTA), and 5 mM HEPES–NaOH, pH 7.4. Flufenamic acid was used to block the conductance caused by removal of external divalent cations (42–44). The hP2X7R-mediated inward currents were elicited by switching for 5 s to the same bath solution containing an additional 0.1 mM free ATP (ATP^{4-}). The interval between ATP applications was 2 min. Each of the three different bath solutions was applied once to the same oocyte in random order. Switching between the different bath solutions was accomplished within <1 s by a set of computer-controlled solenoid valves combined with a modified U-tube technique (8).

Ramp currents were measured during 500-ms-long voltage ramps applied every 1 s between −80 and +40 mV. The holding potential was maintained at −40 mV between ramps. ATP-induced ramp currents were calculated as the difference between the ramp currents before and during ATP application.

Data analysis and presentation

Data were stored and analyzed on a personal computer using software developed in our department (Superpatch 2000, SP-Analyzer by T. Böhm, Julius-Bernstein-Institute of Physiology, Halle, Germany). SigmaPlot (SYSTAT software) was used for fitting, statistical analysis, and data presentation. Statistical data are expressed as mean ± SEM and analyzed by one-way ANOVA. Bonferroni's t-test for multiple comparisons was used to test the statistical significance of differences between means. Statistical significance was set at a P-value of <0.05.

The permeability ratios (P_x/P_y) were calculated from the changes in reversal potential by the Goldman equation (45)

$$\frac{P_X}{P_Y} = e^{\frac{\Delta V_{rev}}{\frac{RT}{F}}} \tag{1}$$

where x and y are cations (Na$^+$ or Tris$^+$) or anions (Cl$^-$ or Glu$^-$), respectively, and ΔV_{rev} is the reversal potential difference measured in extracellular Na$^+$Cl$^-$ versus Tris$^+$Cl$^-$ or Tris$^+$Cl$^-$ versus Tris$^+$-Glu$^-$-based solutions.

The degree of rectification of the *I–V* curves, also known as the rectification index, was calculated as the ratio of the outward to inward conductances, $G_{outward}/G_{inward}$, as described previously (46). The $G_{outward}$ and G_{inward} values were determined from the slopes of the *I–V* curves in the voltage ranges from −75 to −40 and from +20 to +40 mV (SI Appendix, Fig. S6). Voltages > +40 mV were not applied because of their damaging effect on oocytes. When V_{rev} was >+40 mV, it was estimated by extrapolation based on measurements ≤+40 mV.

Results

In silico identification of candidate hP2X7R residues involved in cation selectivity

Like other functional P2XR isoforms (47, 48), the hP2X7R^{wt} assembles as a homotrimer in *X. laevis* oocytes (49). Figure 1A shows a lateral view of a SWISS homology model of the apo-closed homotrimeric hP2X7R^{wt} based on the apo rP2X7R cryo-EM structure (26) with a large extracellular ectodomain containing intersubunit ATP^{4-}-binding sites, a membrane-spanning domain consisting of two transmembrane α-helices per monomer, TM1 and TM2, and a large intracellular domain termed the cytoplasmic ballast (26). The TM1 helices (light gray) face outward. The three central TM2 helices (yellow) form a trihelical bundle that lines the transmembrane pore.

In the "pore" and "membrane ON" modes, where the position of the lipid bilayer is included in the calculation according to the orientations of proteins in membranes (OPM) database (50), the channel prediction tool MOLEonline (33) identifies only a short continuous intramembrane channel pore along the central axis of P2X7R^{wt} in both the apo-closed and ATP-bound open states (Fig. 1B and C), i.e. without any significant access from the outside or exit to the cytoplasm (for calculations with and without membrane constraint, see SI Appendix, Fig. S1). Enlarged views of the TM domains show that residues S339 and S342 (aquamarine and cyan spheres), one per TM2 helix, move laterally to effectively close (Fig. 1B and D) or open (Fig. 1C and E) the channel. The extracellular accessibility of I331 (yellow–orange), V335 (pale yellow), and S339, but not S342, of the closed hP2X7R (Fig. 1B), as shown
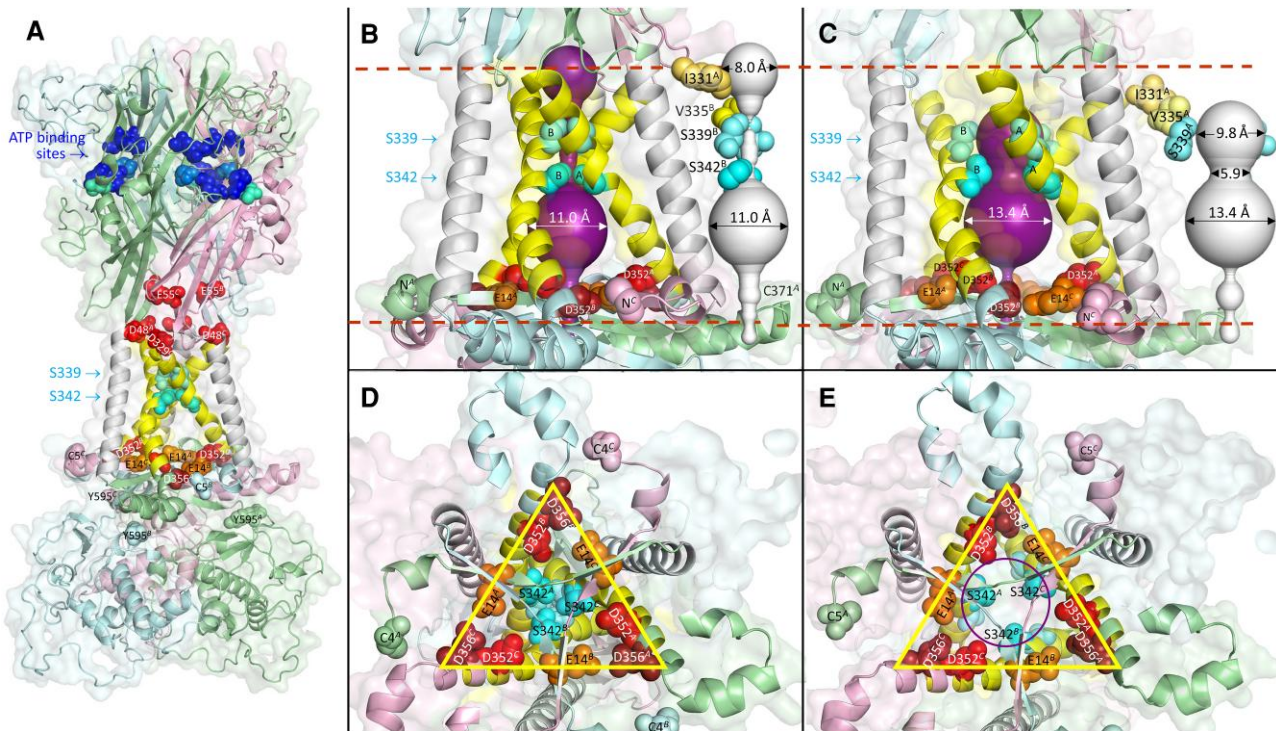
Fig. 1. Visualization of candidate residues involved in controlling the cation selectivity of the hP2X7R. A) Overall structure of the hP2X7R^{wt} homotrimer homology-modeled based on the cryo-EM structure of the apo-closed conformation of the rP2X7R (26), viewed perpendicular to the membrane normal. The hP2X7R^{wt} extends over ~71 (N302^B to D329^C) and ~50 Å (D356^B to S584^B) in the extracellular and intracellular directions, with a maximum width of ~71 Å (G418^B to S290^A). Each of the three identical subunits (ABC) is shown in a different color (A) pale green, B) pale cyan, C) light pink), except for TM1 and TM2, which are shown in white and yellow, respectively, for easier identification. The three TM2 domains line the channel pore. Several residues are highlighted as spheres: C4 and C5, the first residues solved in the apo and open rP2X7R cryo-EM structures, respectively, and the last residue Y595 (corresponding to the C-terminal end) in their chain colors; S339 and S342 around the gate in aquamarine and cyan, respectively; in the ectodomain, the acidic residues in red and the residues that coordinate the ectodomain ATP^{4-} binding by ionic interactions (K64, K66, R294, K311) and hydrogen bonding (T189, N292) in blue and marine, respectively. B), C) Enlarged lateral views of the transmembrane region of the closed and open states of hP2X7R^{wt}, including the channel pore as predicted by MOLEonline (33). Channels are shown in duplicate, with surrounding protein (purple) and, for a free view of the channel shape, in white, with only the selected residues (one or two per triplet) accessible to cysteine-reactive reagents from the extracellular space: I331 (yellow–orange), V335 (pale yellow), S339 (aquamarine), and S342 (cyan). The dashed red lines indicate the outer and cytoplasmic boundaries of the membrane as predicted by the OPM database (50). The open-channel model (C) lacks a sufficiently wide opening to the cytoplasm for ions to exit, as does the closed channel model (B). D), E) Cytoplasmic views on the channel pore and surrounding acidic residues (E14 in orange, D352 in red, D356 in firebrick) at the level of the membrane–cytoplasmic interface after masking of the cytoplasmic structure. Obviously, residues S339 and S342 move laterally to open the pore (compare D to E). In contrast, the acidic residues arranged in an isosceles triangle (yellow) do not move significantly during channel opening (compare D to E).

by cysteine scanning in single-channel and fluorescent dye-binding measurements (27), is consistent with the homology model derived from the cryo-EM structures of rP2X7R (26).

Bounded at the top by S342 in both the closed and open states, there is a voluminous cavity in the second half of the membrane, followed further downstream by an extension into the cytoplasm formed by a ring of three centrally located basic K17 residues that is far too narrow to allow cations to exit into the cytoplasm (Fig. 1B and C, see also SI Appendix, Fig. S2). However, lateral to K17 are nine acidic residues, three per subunit (E14 and D352/D356 each from neighboring subunits), arranged in an isosceles triangle parallel to the membrane to form a massive negative charge cluster that could represent cation selectivity filters (Fig. 1D and E; see also SI Appendix, Fig. S2). Upon ATP^{4-} binding, the channel opens wide due to the lateral movement of S339 and S342, and the voluminous cavity further dilates somewhat, while the lateral nine acidic residues do not move significantly (compare Fig. 1B, D and C, E; SI Appendix, Fig. S2).

Like hP2X7R^{wt}, the gate mutant hP2X7R^{S342K} is cation-selective

The principle of our ion selectivity measurements is shown in Fig. 2. I–V curves were generated during ATP-induced receptor

activation in superfusion solutions containing Na$^+$Cl$^-$ (Fig. 2A–C), Tris$^+$Cl$^-$ (Fig. 2D–F), or Tris$^+$Glu$^-$ (Fig. 2G–I) as major ions. The intersection of the I–V curve with the zero current x-axis yields the reversal potential V_{rev}, which is the potential at which the net current through the open channel is zero. Replacing Na$^+$ (ionic diameter 1.9–2.1 Å) with the three times larger organic cation Tris$^+$ (diameter ~6.4 Å) drastically shifted V_{rev} to the left from −6.8 (Fig. 2A) to −53.9 mV (Fig. 2D) in hP2X7R^{wt}-expressing oocytes. This indicates that most of the current in Fig. 2A was carried by the small cation Na$^+$ and that hP2X7R^{wt} has a much lower permeability for the larger cation Tris$^+$. The calculated Tris$^+$/Na$^+$ permeability ratio P_{Tris}/P_{Na} according to Hille (45) (see Eq. 1) of 0.16 is in good agreement with our previous estimates from single-channel recordings of 0.10 and 0.075 for native hP2X7R in human B lymphocytes (8) and recombinant hP2X7R in *X. laevis* oocytes (10), respectively.

Additional substitution of extracellular Cl$^-$ (ionic diameter 3.6 Å) by the almost 2-fold larger organic anion Glu$^-$ (dimensions 5.5 × 6.5 Å) to test for anion selectivity induced only a slight shift of V_{rev} to more negative potentials from -53.9 mV in Tris$^+$Cl$^-$ (Fig. 2D) to -60.4 mV in Tris$^+$Glu$^-$ (Fig. 2G; not significant, for statistics, see Fig. 3). For an anion-permeable ion channel, one would have
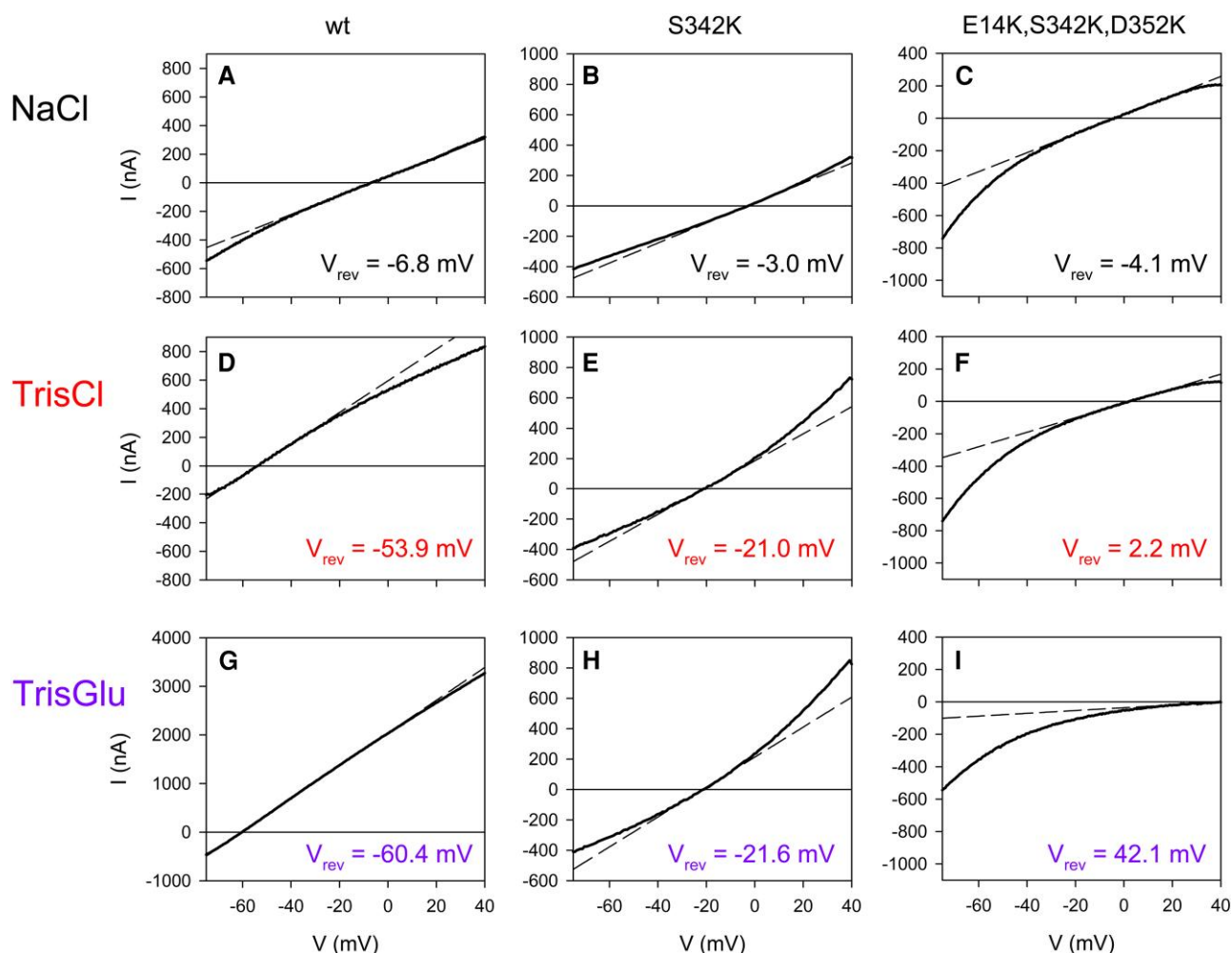
Fig. 2. Ramp currents mediated by hP2X7R^{wt} and mutants expressed in *X. laevis* oocytes. The ATP-induced ramp currents shown were calculated as the difference between the ramp currents before and during 0.1 mM ATP^{-4} application. Only the ramp currents in the voltage range of -70 to +40 mV are shown because capacitive currents are generated by voltage jumps from holding potentials of -40 to -80 mV. The name of the hP2X7R construct expressed is shown at the top of each of the three rows of panels, and the only salt (except ~5 mM HEPES, diameter ~10 Å) of the extracellular solution is shown at the left margin. The bold curved lines show the measured currents; the thin dashed straight lines show the linear fit of the current–voltage relationship near the reversal potential. From this approximation, the V_{rev} values (shown in each of the figures here and in Fig. 3) and the conductance (slope of the lines whose statistics are shown as $G_{at\ Vrev}$ in Fig. 3) were calculated. I) V_{rev} was determined by extrapolation (see Materials and methods). The in-panel numbering (A–H) is used to uniquely identify each panel in the results text description.

expected an opposite shift to more positive reversal potentials (see Fig. 2F and I). The current result is consistent with previous findings that native and recombinant hP2X7R^{wt} is Cl$^-$-impermeable in physiological media (8, 40).

To determine the possible role of the S342 gate (27) in the Na$^+$ versus Cl$^-$ selectivity of hP2X7R, we performed the above protocol on the serine-to-lysine-substituted mutant hP2X7R^{S342K}. The V_{rev} shift of hP2X7R^{S342K} in Na$^+$Cl$^-$ versus Tris$^+$Cl$^-$ was only -18 mV (compare Fig. 2B and E), much smaller than the -48 mV shift observed for hP2X7R^{wt} (compare Fig. 2A and D). The mean calculated permeability ratio P_{Tris}/P_{Na} of 0.52 instead of 0.15 for the wild type (wt) (SI Appendix, Table S1) indicates a reduced but still present preference for Na$^+$ over the bulky Tris$^+$ cation, if the nonhydrated diameter is considered. This could mean that hP2X7R^{S342K} conducts Na$^+$ worse or Tris$^+$ better than hP2X7R^{wt} or both, with the degree of hydration relative to the pore size being a possible reason as suggested by a similar observation with the nicotinic acetylcholine receptor (51). The fully hydrated Na$^+$ cation has a diameter similar to that of Tris$^+$ itself (7.2 versus 5.8–6.8 Å, see Table 1). Why the S342 mutation results in a higher Tris$^+$-to-Na$^+$

permeability ratio, apparently by decreasing Na$^+$ permeation more than Tris$^+$ permeation, is unclear. Specific binding of permeating ions may play a role, presumably because the wt S342 side chains are configured to interact more favorably with permeating hydrated Na$^+$ ions than with Tris$^+$. Alternatively, the reduced pore size due to the S342K mutation may cause Tris$^+$ to act as a "permeant-blocking ion" (19), with Tris$^+$ tightly binding in the pore and sterically hindering Na$^+$ permeation, directly explaining the altered permeability ratio.

After additional substitution of Cl$^-$ by Glu$^-$ in the Tris$^+$-based extracellular solution, V_{rev} remained virtually unchanged from −21.0 (Fig. 2B) to −21.6 mV (Fig. 2C), indicating that the reduced Na$^+$ versus Tris$^+$ preference was not associated with a significant Cl$^-$ permeability of hP2X7R^{S342K}.

The hP2X7R^{E14K,S342K,D352K} triple mutant is an ATP^{4-}-gated anion channel

As suggested from the cryo-EM structure, cations that have passed through the tri-S342 ring exit the central channel through cytoplasmic fenestrations (26). The MOLEonline program also
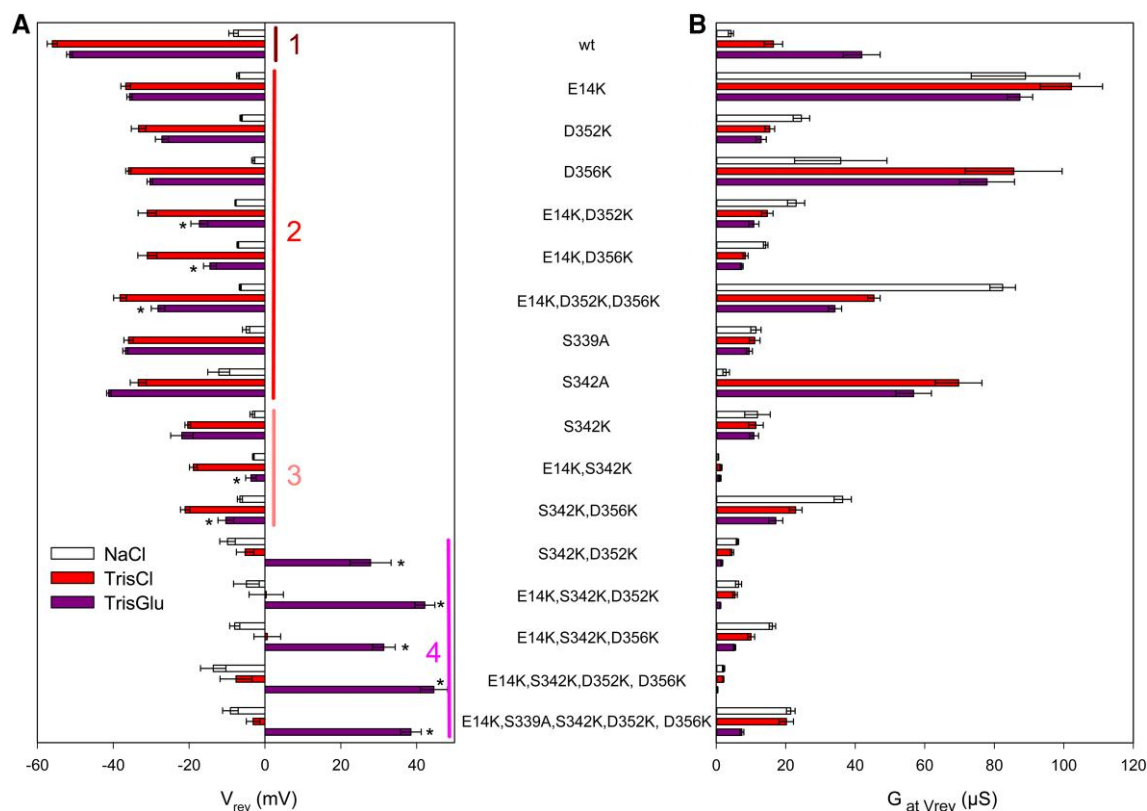
Fig. 3. Permeation characteristics of hP2X7R constructs expressed in *X. laevis* oocytes. The bars represent the reversal potential (A) and the corresponding slope conductance at V_{rev} (B) of the indicated hP2X7R constructs during application of 0.1 mM ATP^{-4} in one of three extracellular solutions based on Na$^+$Cl$^-$ (open columns), Tris$^+$Cl$^-$ (red columns), and Tris$^+$Glu$^-$ (purple columns). Data are mean ± SEM of 6–7 oocytes. A) The constructs are arranged in four correspondingly numbered groups that differ significantly in their reversal potential in Tris$^+$Cl$^-$. Group 1: hP2X7R^{wt}. Group 2: Substitution of single or multiple acidic residues by alanine or lysine as indicated; note that the V_{rev} shift due to substitution of Na$^+$ by Tris$^+$ (i.e. the difference between the white and red columns) of all mutants in this group is significantly smaller than that of hP2X7R^{wt}, indicating that they all have reduced selectivity for small cations. Group 3: Note that the S^{342}K mutation further reduces the V_{rev} shift in Tris$^+$Cl$^-$ versus NaCl compared to the mutants in group 2, indicating a further reduced selectivity for the small cation Na$^+$; the additional mutation of E14 or D356 to lysine additionally produces a significant V_{rev} shift in Tris$^+$Glu$^-$ versus Tris$^+$Cl$^-$, most likely reflecting an occurring anion permeability with reduced permeability to Glu$^-$ compared to Cl$^-$. Group 4: Na$^+$ substitution by Tris$^+$ has no effect on V_{rev}, indicating a loss of cation permeability. The V_{rev} shift in Tris$^+$Glu$^-$ versus Tris$^+$Cl$^-$ was further strongly increased when the S^{342}K mutation was combined either with D^{352}K alone or with E^{14}K and D^{356}K together, an effect that could not be surpassed by mutating all three acidic residues to lysines or by additionally incorporating the S^{339}A mutation.

predicts, with variable frequency and also depending on the homology mutant analyzed (almost 100% for hP2X7R^{E14K}), lateral pathways from the large cavity below S342 lined by acidic residues such as E14 and D352 at the intracellular membrane interface of hP2X7R^{wt} (SI Appendix, Fig. S3). To determine the role of these conserved lateral acidic residues on ion selectivity, we mutated E14 and D352 to lysine together with the tri-S342 gate, yielding hP2X7R^{E14K,S342K,D352K}. Replacing Na$^+$ with Tris$^+$ caused a statistically insignificant shift of V_{rev} of hP2X7R^{E14K,S342K,352K} toward positive values (compare Fig. 2C and F; for statistical analysis, see Fig. 3). This suggests that the E^{14}K, S^{342}K, D^{352}K mutation either eliminated the inherent cation selectivity of hP2X7R^{wt}, or at least its preference for the small cation Na$^+$ over the larger Tris$^+$. Consistent with a complete loss of cation permeability, the additional substitution of extracellular Cl$^-$ by the twice as large Glu$^-$ was accompanied by a large positive V_{rev} shift of +39.9 mV (Fig. 2I), indicating a 4.8-fold greater Cl$^-$ than Glu$^-$ permeability (P_{Glu}/P_{Cl} of 0.21, mean 0.22 ± 0.05, see SI Appendix, Table S1). It follows that lysine substitution of E14 and D352 (in addition to S342) in hP2X7R^{E14K,S342K,352K} results in selectivity for the small anion Cl$^-$, in contrast to hP2X7R^{wt} and hP2X7R^{S342K}, which are equally impermeable to Cl$^-$ and Glu$^-$. Both together, the insignificant V_{rev} shift due to Na$^+$ by Tris$^+$ substitution and the strong positive

shift due to Cl$^-$ by Glu$^-$ substitution, are typical features of anion-selective ion channels such as the volume-regulated anion channel (52). We conclude that the hP2X7R^{E14K,S342K,D352K} mutant behaves like an ATP^{4-}-gated anion channel.

Acidic residues at the cytoplasmic exit of the TM2 channel control cation selectivity

To elucidate the individual contribution of the lysine substitutions of residues E14, S342, and D352 to the altered charge selectivity, we substituted each of these residues individually and in various combinations with lysines, including the nonconserved residue D356 and also S339, one helical turn above the gating residue S342 (see Fig. 1). Since S339K mutants were generally not functional (see also SI Appendix, Fig. S4), we had to make do with alanine mutants at this position. The reversal potentials were determined using the protocol described in Fig. 2. The data are summarized in Fig. 3A, sorted into four groups with comparative statistical analysis.

Group 1 shows the mean V_{rev} values of hP2X7R^{wt} in Na$^+$Cl$^-$ (white bar), Tris$^+$Cl$^-$ (red bar), and Tris$^+$Glu$^-$ (purple bar). Group 2 shows the V_{rev} values of hP2X7R mutants with single, double, and triple lysine substitutions of E14, D352, or D356. Each single

lysine substitution as well as the single S339A and S342A mutations within this group consistently resulted in a less negative V_{rev} in Tris$^+$Cl$^-$ (red bars) compared to hP2X7R^{wt}. This indicates that each of the five mutations reduced the preference for Na$^+$ relative to Tris$^+$, but Na$^+$ was always preferred to Tris$^+$ according to the still negative V_{rev} shift induced by the substitution of Na$^+$ by Tris$^+$.

Replacing Tris$^+$Cl$^-$ with Tris$^+$Glu$^-$ did not significantly reduce the V_{rev} of the single mutants, indicating that the anion exclusion typical of hP2X7^{wt} is maintained (compare red and purple bars). However, when the E^{14}K mutation was combined with D^{352}K or/and D^{356}K mutations, V_{rev} shifted statistically significantly to the positive in Tris$^+$Glu$^-$, i.e. when Cl$^-$ was replaced by the organic anion Glu$^-$ (compare height of purple versus red bars in Fig. 3A). This indicates that replacement of two or three acidic residues at the membrane–cytoplasmic interface of each subunit with lysines renders hP2X7R anion permeable.

Because of the relatively strong effect of the S^{339}A and S^{342}A mutations on ion selectivity (group 2), we tested the introduction of a positive charge at position S339 or S342 by mutating serine to lysine. The S^{339}K single mutant was nonfunctional, although an E^{14}K, S^{339}K double mutant was weakly expressed in the plasma membrane (see SI Appendix, Fig. S5A). In contrast, the S^{342}K single mutation was functional and resulted in a less negative V_{rev} shift than any of the E^{14}K, D^{352}K, or D^{356}K single mutations in group 2 when Na$^+$ was replaced by Tris$^+$ (heights of red versus white bars). This suggests that S342 contributes significantly more to the small cation Na$^+$ versus Tris$^+$ selectivity of hP2X7R than either E^{14}, D^{352}, or D^{356} alone. This is best explained by S342 acting primarily as a size-selective filter, reducing the permeation of larger cations such as Tris$^+$. The combination of the S^{342}K mutation with either the E^{14}K or D^{356}K mutation resulted in anion permeability, as evidenced by the statistically significant positive shift of V_{rev} upon Cl$^-$ to Glu$^-$ substitution. Mutants with these properties were assigned to the new group 3.

Since hP2X7R^{S339K} was not functional as an ATP^{4-}-gated channel, we also examined the alanine mutant hP2X7R^{S339A} in the context of E^{14}K, D^{356}K. hP2X7R^{E14K,S339A,D356} was functional but had no further effect on V_{rev} when combined with E^{14}K and S^{342}K (Fig. 3A). This suggests a negligible contribution of the hydroxyl side chain of S339 to the ion selectivity of hP2X7R.

The combination of the S^{342}K and D^{352}K mutations in hP2X7^{S342K,D352K} resulted in an even further shift to more positive V_{rev} values in Tris$^+$Cl$^-$ so that they were no longer different from the values in Na$^+$Cl$^-$ and were therefore assigned to group 4 (Fig. 3A). Furthermore, a particularly strong shift of V_{rev} to high positive voltages occurred here when Cl$^-$ was replaced by Glu$^-$ (compare the height of the purple bars between groups 3 and 4). The positive V_{rev} shift was further increased by including the E^{14}K mutation in the triple mutant hP2X7^{E14K,S342K,D352K}, whereas the triple mutant hP2X7^{E14K,S342K,D356K} was approximately equivalent to the double mutant hP2X7^{S342K,D352K}. Taken together, this suggests that D352 is more important for ion selectivity than E14 or D356, both of which had to be simultaneously mutated to lysines to have the same effect as D^{352}K when combined with S^{342}K. The lack of effect of the Na$^+$ to Tris$^+$ substitution on V_{rev} combined with the simultaneous strong shift of V_{rev} to positive potentials in Tris$^+$Glu$^-$ indicates that all group 4 hP2X7R mutants are purely selective for the small Cl$^-$ anion.

A complete shift from cation to anion permeability was also induced by mutation of D352 or/and D356 in the E^{14}K, S^{342}K background. Again, the additional alanine mutation of S339, which is one helical turn upstream of S342 and, like S342, is located in the narrowest region of the closed trihelical TM2 channel (Fig. 1), had no additional effect on the positive V_{rev} shift induced by the Cl$^-$ to Glu$^-$ substitution (Fig. 3). This supports our previous single-channel data that S339 does not act as a selectivity filter (27), and is also consistent with the cryo-EM structure and our derived homology models showing that the open pore diameter is significantly larger above and below the triple S342 ring, except for the constriction at K17, which can be ruled out as an exit site (see SI Appendix, Fig. S2). Unfortunately, the nonfunctional state of hP2X7R^{S339K} did not allow a more comprehensive analysis. The alanine and lysine mutants of Y343, next to S342 in the ion channel, were also not functionally expressed, although at least hP2X7R^{E14K,Y343K} was expressed at the plasma membrane (SI Appendix, Fig. S5C). The permeability ratios reflecting the V_{rev} shifts of all hP2X7R mutants examined are summarized with statistical analysis in SI Appendix, Table S1.

The ATP^{4-}-induced conductances ($G_{at\ Vrev}$) of all hP2X7R constructs are shown in Fig. 3B. The ATP^{4-}-induced conductances differed greatly between the different hP2X7R mutants. The use of conductance has the advantage of being independent of membrane potential. In addition, according to the Goldman equation, the reversal potential across a homogeneous population of ion channels is independent of the expression level. Overall, the presence of the S342K or/and D352 mutation strongly reduced the conductance of the respective construct, which in the case of the S342K mutation can be well correlated with the strong reduction of the narrowest part of the wt pore from 6.0 to 3.3 and 3.0 Å for the mutants S342K and E14K, S342K, D352K, and D356K, respectively (SI Appendix, Fig. S4).

Virtually all hP2X7R mutants examined (with the exception of two nonfunctional mutants) were consistently well expressed at plasma membrane in the three biochemical experiments shown (SI Appendix, Fig. S5A–C). The maximum plasma membrane variation by a factor of 2 is much too small to be considered a major cause of the conductance variations. Therefore, the most likely explanation for the functional differences is that the open probabilities and/or single-channel conductances of the different mutants are significantly different.

Mutation of acidic residues to lysine at the cytoplasmic interface causes strong inward rectification

The I–V curves in Fig. 2A, D, and G show a nearly linear current–voltage relationship for ATP^{4-}-induced currents mediated by hP2X7R^{wt}, indicating little or no rectification. This is consistent with previous measurements in both whole-cell mode (5, 8) and single-channel mode (10, 40, 53). In contrast, the I–V curves for hP2X7R^{S342K} (Fig. 2H) show strong outward rectification, which was reversed to inward rectification by additional lysine substitutions of E14 and D352 in the triple mutant hP2X7R^{E14K,S342K,D352K} (Fig. 2I). To systematically examine the correlation, we quantified the rectification index for hP2X7R^{wt} and all its mutants as the ratio of the slope conductance at negative and positive potentials in all three extracellular solutions (see Materials and methods), as shown as examples for hP2X7R^{S342K} and hP2X7R^{E14K,S342K,D352K} (SI Appendix, Fig. S6A and B, respectively). Statistics are presented as bar graphs (SI Appendix, Fig. S6C). In almost all constructs summarized as group 2 in Fig. 3A, outward rectification increased significantly when Na$^+$ was replaced by Tris$^+$. This can be explained by a decrease in the inward current, which is now carried by the larger, less permeable Tris$^+$ ion instead of Na$^+$, providing additional evidence for small cation selectivity. The strong inward rectification of the hP2X7R^{E14K,S342K,D352K} mutant in Tris$^+$Glu$^-$ (reflected

by the absence of outward current at positive potentials up to +40 mV) can be explained by the absence of available charge carriers: endogenous intracellular Cl^- can move out at negative potentials, but Glu^- cannot enter because of its larger size.

Effect of lysine mutations on pore diameter and shape by homology modeling and structural visualization

A compilation of SWISS homology-modeled pore sections shows that the isosceles triangular arrangement of residues is preserved in all 17 electrophysiologically characterized hP2X7R mutants, even with multiple lysine substitutions. The open states of wt and five of these mutants are exemplarily shown in SI Appendix, Fig. S4, in top (A–F) and bottom views (G–L) together with the modeled pores (M–R). The S342K mutation (SI Appendix, Fig. S4, compare A–C with D and E), but not the nonfunctional S339K mutation (SI Appendix, Fig. S4, compare A with F), reduced the visible pore diameter at the level of residue 342 by about half (from 6.0 Å to 3.0–3.3 Å). In contrast, pore diameter at residue 342 was unaffected by multiple acid-to-lysine mutations in the acidic triangle (SI Appendix, Fig. S4, compare A–C).

Discussion

Based on the structure of the truncated homotrimeric zebrafish P2X4R (54, 55), the narrowest part of the ATP-gated ion-conducting pathway is formed by the trihelical TM2 bundle, as confirmed by functional experiments (56) and also by the cryo-EM structure of rP2X7R (26). In hP2X7R, we found the tri-S342 ring in TM2 to be involved in gating and permeation, acting as a size-selective filter (27). In addition, we show in this work that the S342K mutation only affects the relative selectivity for Na^+ versus $Tris^+$, which have effective diameters of 1.9 versus 6.5 Å, respectively, but does not itself induce anion permeability. This is in contrast to the reported importance of the equivalent residue Thr339 in rat P2X2R, which when mutated to lysine changed permeation from 10-fold cation selective to anion preferential (57).

Acidic isosceles triangle: a large-diameter, high-field electrostatic cation selectivity filter for small inorganic and small organic cations

In our previous SCAM experiments (27), we observed that the membrane-impermeant anionic cysteine-reactive 5.8 Å reagent $MTSES^-$ reacted with S342C when applied externally, but not when applied to the cytosolic side. In contrast, the cationic 5.8 Å reagent $MTSET^+$ reacted with S342C from both sides of the membrane. A logical explanation for this difference is the presence of a true cation-selective filter downstream of S342 that is impenetrable to the $MTSES^-$ anion from the cytosolic side. Based on the recognition of the closely spaced acidic residues E14, D352, and D356 deep in the membrane at the cytoplasmic interface, we were able to gradually shift the permeation properties of hP2X7R from cation to anion selectivity by stepwise mutation of the acidic residues to lysines. The importance of basic residues as anion selectivity filters is well known for instance for TMEM16A Ca^{2+}-activated Cl^- channels (58).

Considering the ability of the 5.8-Å-diameter $MTSET^+$ to react "backwards" with $S^{342}C$ when applied cytosolically (27), we can retrospectively conclude that the acidic cation selectivity filter at the channel exit must also have a diameter of at least 5.8 Å. Calculation of the mean distances by PyMOL between the carboxyl groups of E14 and D352 and E14 and D356 of the homology-

modeled hP2X7R mutants gave 9.6 ± 1.5 and 5.4 ± 0.5 Å ($\pm$SD), respectively, and 7.4 ± 2.5 Å ($\pm$SD) overall, which is in the range consistent with anterograde $Tris^+$ and retrograde $MTSET^+$ permeation. We propose that the high density of three negative charges per lateral pore at the interface of two subunits is necessary to generate an electrostatic field strong enough to force selectivity even for solvated cations. In other words, the high charge density serves to compensate for the large pore radius. This view is supported by our observation that all three acidic residues (together with the size filter at S342) are necessary for pure cation selectivity and that this selectivity gradually disappears with each acidic residue mutated to a lysine.

The Tri-S342 ring in the center of the membrane is primarily a size filter for cations

The S342K mutation reduced the modeled pore size to 3.3 Å (SI Appendix, Fig. S4), which is close to the 3.6 Å ionic diameter of dehydrated Cl^-. Therefore, we expected that the combination of a pore size close to Cl^- combined with the introduced positive charge alone would convert the hP2X7R from Na^+ to Cl^- permeability. However, no detectable anion permeability was seen with the S342K mutation alone. How the S342K mutation, together with the lysine substitutions in the acidic triangle, contributes to Cl^- selectivity remains unclear at this time. One speculative possibility is that any Cl^- that winds through the narrow pore of the ^{S342K}hP2X7R single mutant cannot pass further because its passage is electrostatically blocked by the acidic residues E14/D352/D356, i.e. selectivity filter 2. Only the lysine mutation of both selectivity filters allows the unhindered flow of Cl^-. This view is supported by the observation that the opposite is also true: the charge reversal mutations in the acidic triangle alone result in a certain Cl^- permeability, as can be seen from group 2 in Fig. 2. This suggests that Cl^- could in principle even pass through $hP27R^{wt}$ S342 selectivity filter, but again its passage is electrostatically blocked by the acidic selectivity filter 2. Therefore, a primary size filter with a possible effect on the hydration of the permeating ions seems to be the most likely role for S342 at this time.

Role of acidic residues in the TM2 of P2XRs in relation of literature

The basic data of this work are graphically summarized in Fig. 4. Based on the insight that the arrangement of acid residues in the cytoplasmic interface may serve as a selectivity filter, we were able to gradually change the permeation characteristics from selectivity for small cations ($hP2X7R^{wt}$) to selectivity for small anions (e.g. $hP2X7R^{E14K,S342K,D352K}$). The virtual impermeability to anions provides additional support for the view that the proposed dilation of the P2X7R ion channel pore, reportedly associated with the ion channel becoming nonselective also for large organic cations (5, 60) and anions (61), is an artifact. Our new data re-emphasize the view that the hP2X7R maintains a stable conductance for cations with a minimum cross-sectional diameter < 8.5 Å (10, 27), but is per se impermeable to anions (8) (40).

Here, we show that in addition to S342 of TM2, ions are selected by acidic amino acid residues (E14, D352 and D356) along the lateral pores of the cytoplasmic part of the hP2X7R protein. Lysine mutations at S342 and at the critical lateral pore residues produced ion channels with currents independent of extracellular cations, indicating a loss of cation permeability. Instead, currents using the "new" selectivity filters at K342 and K352 (or additionally at K14 and K356) are dependent on the size of the extracellular
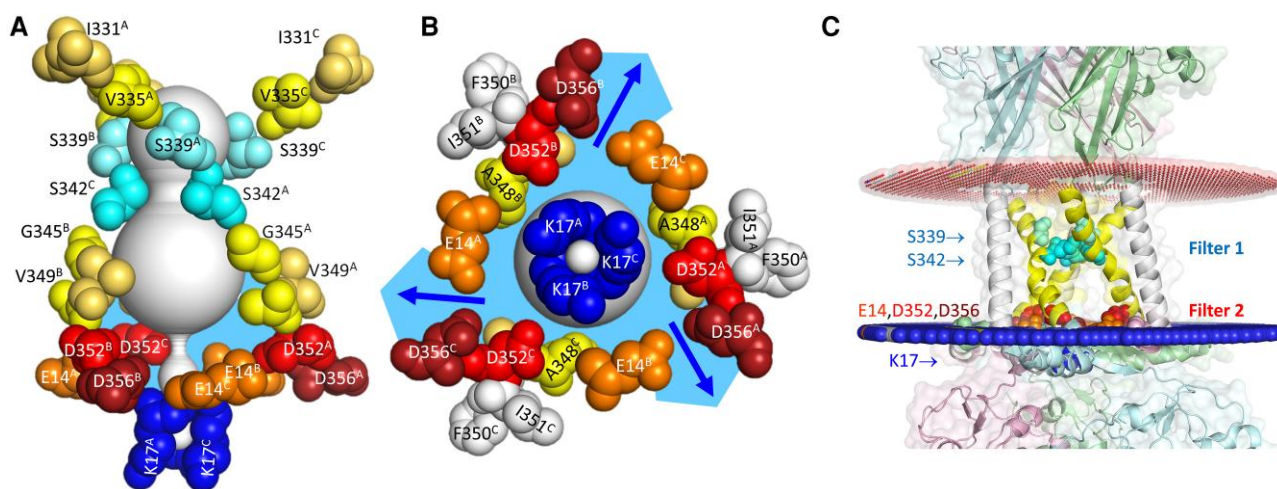
Fig. 4. Cation selectivity filter at the cytoplasmic interface of hP2X7R^{wt}. Lateral (A) and bottom (B) views of the open hP2X7R^{wt} with labeled residues lining the open pore or located more peripherally (F350, I351, colored gray). The pore was modeled using MOLEonline. From the frequent detection of single lateral pores in the open hP2X7R channel by the MOLEonline software (see SI Appendix, Fig. S3) and consistent with the data shown here, we conclude that the fluid in the cavity below the tri-S342 ring (sky blue) and the lateral pores is continuum, with access controlled by the gate at S342 (selectivity filter 1). C) Location of filters 1 and 2 relative to phospholipid head groups. Our electrophysiological data indicate that cations exit through three exits (indicated by blue arrows), one between each subunit interface and each flanked by E14 of one subunit and D352/D356 of the adjacent subunit (size-selective filter 2). The membrane boundaries of the SWISS homology-modeled open hP2X7R^{wt} were determined using the "OPM" server (https://opm.phar.umich.edu/) with the conditions "Mammalian plasma membrane," "Allow curvature yes," "Topology N-term in" (50, 59). The red and blue pseudo-atoms were automatically added by the OPM server to mark the hydrophobic boundaries of the lipid bilayer. The downloaded PDF file was visualized with PyMOL. Note the proximity of the cation selectivity filter to the phospholipid headgroups and the apparent lack of coverage of the transmembrane channel by the main and side chains of flanking amino acid residues, both of which may be related to the effect of lipids on ion permeation (25) (channel portion in A) uncovered by amino acid main and side chains).

anion, i.e. the filters allow Cl$^-$ (effective diameter 3.6 Å) to permeate more easily than the bulkier Glu$^-$ (effective diameter 5.5 Å).

The lateral pores are part of the cytoplasmic cap (26) and allow ions to exit the large cavity below S342 in the cytoplasmic half of the membrane through the size-selective filter into the cytoplasm. However, a complete reversal of charge selectivity from cationic to anionic required mutations of S342 and at least D352 to lysine, suggesting that the cation selectivity of hP2X7R is a product of the combination of the two filters.

Our results indicate that D352 of P2X7R or equivalent positions of other P2XRs are critical for P2XR ion permeation. It has been suggested previously that ion flow through P2Xs into the cytoplasm does not occur along the central axis of the cytoplasmic domain, but through lateral fenestrations (26, 62), but which amino acid residues line these pores remained unresolved. Several previous reports support our view of the important role of D352 in the P2X7R ion permeation pathway. Single-channel currents of rat P2X2R were abolished when residue D349, corresponding to D352 in hP2X7R (and D361 in the 12 N-terminal residues longer hP2X2R, SI Appendix, Fig. S7), was replaced by neutral or positively charged residues (63). rP2X2R^{D349C} mediated only small currents after activation by ATP (64) and was blocked by MTSEA$^+$ (65) or Cd^{2+} (66). These results indicated early on that this position is critical for ion permeation. Furthermore, hP2X7R^{D352C} mediated only 10% of the hP2X7R^{wt} conductance (27). Substitution of T348 and D352 with basic residues in the channel-lining TM2 domain of the rP2X7R simultaneously increased the permeability of the normally cationic channel for Cl$^-$ and an acidic fluorescent dye with an effective diameter of >10 Å (61).

Residues equivalent to E14 of hP2X7R were previously identified as critical for the cation selectivity of rat P2X2 (E17) and the additional anion permeability of mouse P2X5 (K17), as well as for the access to the transmembrane pore through lateral fenestrations (31). The importance of E14 for the Ca^{2+} permeability of rP2X7R has already been shown (67). In an alternatively spliced

version of P2X7 (P2X7k (68)), the acidic E14 is replaced by the neutral asparagine residue. This leads to a shift of the reversal potential to more positive potentials in NMDG$^+$ containing extracellular solution. The fractional P2X7k-mediated Ca^{2+} current is reduced compared to hP2X7^{wt} (67). These results previously suggested that the N-terminal E14 residue is important for the permeation properties of hP2X7R.

The involvement of lateral fenestrations in the extracellular domain in the ion selection process has been proposed for the P2X4R (69–71). Although ions may use a similar pathway in P2X7R-mediated currents, the extracellular pores appear to be irrelevant for the cation selectivity of P2X7R, since the combined mutation at the two filter sites, S342 and acidic triangle, is sufficient to completely alter the charge selectivity of hP2X7R ions.

All these previous findings, together with our results shown here, support our view that ion selection of P2X7Rs occurs in a two-step fashion, with (i) a size-selective filter located in the middle of the TM2 domain and (ii) acidic residues lining lateral fenestrations controlling cation flow from the bulky cavity in the cytoplasmic half of the membrane into the cytoplasm (see graphical summary in Fig. 4). The conservation of D352 across the P2XR family (SI Appendix, Fig. S7; see also a comprehensive interspecies P2X sequence alignment in (54)) suggests that the cation selectivity of P2XR generally involves the mechanism described here.

Acknowledgments

Supplementary Material

Supplementary material is available at *PNAS Nexus* online.

Author Contributions

F.M. and G.S. Conceptualization, Data curation, Formal analysis, Funding acquisition, Investigation, Methdology, Project administration, Resources, Supervision, Visualization, Writing-original draft, Writing-reviewing & editing. E.C.S. Investigation, Formal analysis; M.R., A.M., S.H.Y., and M.B. Investigation.

Preprints

This manuscript was posted on a preprint: https://www.biorxiv.org/content/10.1101/2024.02.19.579953v1.

Data Availability

All data are included in the manuscript and/or supporting information. In addition, the dataset used for the statistical analysis of Fig. 3 is deposited in the Open Access Research Data Repository "Share_it" of the University Libraries of Saxony-Anhalt.

Institutional Review Board Statement

The procedures for maintenance of the frogs and their ovariectomy were approved by the local animal welfare committees (Halle, Germany, reference no. Az. 203.42502-2-1493 MLU, and Düsseldorf, Germany, reference no. 8.87-51.05.20.10.131 for experiments performed in Halle and Aachen, respectively) in compliance with the EC Directive 86/609/EEC for animal experiments.

References

1. Schmidt S, Isaak A, Junker A. 2023. Spotlight on P2X7 receptor PET imaging: a bright target or a failing star? *Int J Mol Sci*. 24:1374.

2. Collo G, *et al.* 1997. Tissue distribution of the P2X7 receptor. *Neuropharmacol*. 36:1277–1283.

3. Di Virgilio F, Sarti AC, Falzoni S, De Marchi E, Adinolfi E. 2018. Extracellular ATP and P2 purinergic signalling in the tumour microenvironment. *Nat Rev Cancer*. 18:601–618.

4. Di Virgilio F, Schmalzing G, Markwardt F. 2018. The elusive P2X7 macropore. *Trends Cell Biol*. 28:392–404.

5. Surpranant A, Rassendren F, Kawashima E, North RA, Buell G. 1996. The cytolytic P2Z receptor for extracellular ATP identified as a P2X receptor (P2X7). *Science*. 272:735–738.

6. Verhoef PA, Estacion M, Schilling W, Dubyak GR. 2003. P2X7 receptor-dependent blebbing and the activation of Rho-effector kinases, caspases, and IL-1 beta release. *J Immunol*. 170:5728–5738.

7. Morelli A, *et al.* 2003. Extracellular ATP causes ROCK I-dependent bleb formation in P2X7-transfected HEK293 cells. *Mol Biol Cell*. 14:2655–2664.

8. Bretschneider F, Klapperstück M, Lohn M, Markwardt F. 1995. Nonselective cationic currents elicited by extracellular ATP in human B-lymphocytes. *Pflügers Arch*. 429:691–698.

9. Riedel T, Lozinsky I, Schmalzing G, Markwardt F. 2007. Kinetics of P2X7 receptor-operated single channels currents. *Biophys J*. 92:2377–2391.

10. Riedel T, Schmalzing G, Markwardt F. 2007. Influence of extracellular monovalent cations on pore and gating properties of P2X7 receptor-operated single-channel currents. *Biophys J*. 93:846–858.

11. Shannon RD. 1976. Revised effective ionic radii and systematic studies of interatomie distances in halides and chaleogenides. *Acta Crystallogr*. A32:751–767.

12. Nightingale ER. 1959. Phenomenological theory of ion solvation. Effective radii of hydrated ions. *J Phys Chem*. 63:1381–1387.

13. Mancinelli R, Botti A, Bruni F, Ricci MA, Soper AK. 2007. Hydration of sodium, potassium, and chloride ions in solution and the concept of structure maker/breaker. *J Phys Chem B*. 111:13570–13577.

14. Pauling L. 1960. *The nature of the chemical bond and the structure of molecules and crystals: an introduction to modern structural chemistry. The George Fisher Baker non-resident lectureship in chemistry at Cornell University*. 3rd ed. Ithaca (NY): Cornell University Press. p. 644.

15. Varma S, Rempe SB. 2006. Coordination numbers of alkali metal ions in aqueous solutions. *Biophys Chem*. 124:192–199.

16. Mähler J, Persson I. 2012. A study of the hydration of the alkali metal ions in aqueous solution. *Inorg Chem*. 51:425–438.

17. Franciolini F, Nonner W. 1987. Anion and cation permeability of a chloride channel in rat hippocampal neurons. *J Gen Physiol*. 90:453–478.

18. Klein H, *et al.* 2007. Structural determinants of the closed KCa3.1 channel pore in relation to channel gating: results from a substituted cysteine accessibility analysis. *J Gen Physiol*. 129:299–315.

19. Villarroel A, Burnashev N, Sakmann B. 1995. Dimensions of the narrow portion of a recombinant NMDA receptor channel. *Biophys J*. 68:866–875.

20. Virginio C, MacKenzie A, Rassendren FA, North RA, Surprenant A. 1999. Pore dilation of neuronal P2X receptor channels. *Nat Neurosci*. 2:315–321.

21. Huang LY, Catterall WA, Ehrenstein G. 1979. Comparison of ionic selectivity of batrachotoxin-activated channels with different tetrodotoxin dissociation constants. *J Gen Physiol*. 73:839–854.

22. Oyane A, *et al.* 2003. Formation and growth of clusters in conventional and new kinds of simulated body fluids. *J Biomed Mater Res A*. 64:339–348.

23. Li M, Toombes GE, Silberberg SD, Swartz KJ. 2015. Physical basis of apparent pore dilation of ATP-activated P2X receptor channels. *Nat Neurosci*. 18:1577–1583.

24. Harkat M, *et al.* 2017. On the permeation of large organic cations through the pore of ATP-gated P2X receptors. *Proc Natl Acad Sci U S A*. 114:E3786–E3795.

25. Karasawa A, Michalski K, Mikhelzon P, Kawate T. 2017. The P2X7 receptor forms a dye-permeable pore independent of its intracellular domain but dependent on membrane lipid composition. *Elife*. 6:e31186.

26. McCarthy AE, Yoshioka C, Mansoor SE. 2019. Full-length P2X7 structures reveal how palmitoylation prevents channel desensitization. *Cell*. 179:659–670.e13.

27. Pippel A, *et al.* 2017. Localization of the gate and selectivity filter of the full-length P2X7 receptor. *Proc Natl Acad Sci U S A*. 114:E2156–E2165.

28. Degrève L, Vechi SM, Junior CQ. 1996. The hydration structure of the Na$^+$ and K$^+$ ions and the selectivity of their ionic channels. *Biochim Biophys Acta*. 1274:149–156.

29. Bo X, *et al.* 2003. Pharmacological and biophysical properties of the human P2X5 receptor. *Mol Pharmacol*. 63:1407–1416.

30. Schiller IC, *et al.* 2022. Dihydropyridines potentiate ATP-induced currents mediated by the full-length human P2X5 receptor. *Molecules*. 27:1846.

31 Tam SW, Huffer K, Li M, Swartz KJ. 2023. Ion permeation pathway within the internal pore of P2X receptor channels. *Elife*. 12: e84796.

32 Larkin MA, *et al.* 2007. Clustal W and Clustal X version 2.0. *Bioinformatics*. 23:2947–2948.

33 Pravda L, *et al.* 2018. MOLEonline: a web-based tool for analyzing channels, tunnels and pores (2018 update). *Nucleic Acids Res*. 46: W368–W373.

34 Gloor S, Pongs O, Schmalzing G. 1995. A vector for the synthesis of cRNAs encoding Myc epitope-tagged proteins in *Xenopus laevis* oocytes. *Gene*. 160:213–217.

35 Klapperstück M, Büttner C, Schmalzing G, Markwardt F. 2001. Functional evidence of distinct ATP activation sites at the human P2X(7) receptor. *J Physiol*. 534:25–35.

36 Weiner MP, *et al.* 1994. Site-directed mutagenesis of double-stranded DNA by the polymerase chain reaction. *Gene*. 151: 119–123.

37 Schmalzing G, Markwardt F. 2022. Established protocols for cRNA expression and voltage-clamp characterization of the P2X7 receptor in *Xenopus laevis* oocytes. *Methods Mol Biol*. 2510: 157–192.

38 Fallah G, *et al.* 2011. TMEM16A(a)/anoctamin-1 shares a homodimeric architecture with CLC chloride channels. *Mol Cell Proteomics*. 10:M110.004697.

39 Fischer L, *et al.* 2023. Physiologically relevant acid-sensing ion channel (ASIC) 2a/3 heteromers have a 1:2 stoichiometry. *Commun Biol*. 6:701.

40 Kubick C, Schmalzing G, Markwardt F. 2011. The effect of anions on the human P2X7 receptor. *Biochim Biophys Acta*. 1808: 2913–2922.

41 Neher E. 1992. Ion channels for communication between and within cells. *Science*. 256:498–502.

42 Weber WM, Liebold KM, Reifarth FW, Clauss W. 1995. The Ca2+-induced leak current in *Xenopus* oocytes is indeed mediated through a Cl− channel. *J Membr Biol*. 148:263–275.

43 Klapperstück M, Büttner C, Böhm T, Schmalzing G, Markwardt F. 2000. Characteristics of P2X7 receptors from human B lymphocytes expressed in *Xenopus* oocytes. *Biochim Biophys Acta*. 1467: 444–456.

44 Klapperstück M, *et al.* 2000. Antagonism by the suramin analogue NF279 on human P2X1 and P2X7 receptors. *Eur J Pharmacol*. 387: 245–252.

45 Hille B. 1971. The permeability of the sodium channel to organic cations in myelinated nerve. *J Gen Physiol*. 58:599–619.

46 Stolz M, *et al.* 2015. Homodimeric anoctamin-1, but not homodimeric anoctamin-6, is activated by calcium increases mediated by the P2Y1 and P2X7 receptors. *Pflugers Arch*. 467:2121–2140.

47 Nicke A, *et al.* 1998. P2x1 and P2X3 receptors form stable trimers: a novel structural motif of ligand-gated ion channels. *EMBO J*. 17: 3016–3028.

48 Aschrafi A, Sadtler S, Niculescu C, Rettinger J, Schmalzing G. 2004. Trimeric architecture of homomeric P2X2 and heteromeric P2X1+2 receptor subtypes. *J Mol Biol*. 342:333–343.

49 Becker D, *et al.* 2008. The P2X7 carboxyl tail is a regulatory module of P2X7 receptor channel activity. *J Biol Chem*. 283: 25725–25734.

50 Lomize MA, Pogozheva ID, Joo H, Mosberg HI, Lomize AL. 2012. OPM database and PPM web server: resources for positioning of proteins in membranes. *Nucleic Acids Res*. 40:D370–D376.

51 Cohen BN, Labarca C, Czyzyk L, Davidson N, Lester HA. 1992. Tris+/Na+ permeability ratios of nicotinic acetylcholine receptors

52 Burow P, Klapperstück M, Markwardt F. 2015. Activation of ATP secretion via volume-regulated anion channels by sphingosine-1-phosphate in RAW macrophages. *Pflugers Arch*. 467:1215–1226.

53 Markwardt F, Lohn M, Böhm T, Klapperstück M. 1997. Purinoceptor-operated cationic channels in human B lymphocytes. *J Physiol*. 498 (Pt 1):143–151.

54 Kawate T, Michel JC, Birdsong WT, Gouaux E. 2009. Crystal structure of the ATP-gated P2X4 ion channel in the closed state. *Nature*. 460:592–598.

55 Hattori M, Gouaux E. 2012. Molecular mechanism of ATP binding and ion channel activation in P2X receptors. *Nature*. 485:207–212.

56 Peverini L, Beudez J, Dunning K, Chataigneau T, Grutter T. 2018. New insights into permeation of large cations through ATP-gated P2X receptors. *Front Mol Neurosci*. 11:265.

57 Browne LE, *et al.* 2011. P2x receptor channels show threefold symmetry in ionic charge selectivity and unitary conductance. *Nat Neurosci*. 14:17–18.

58 Peters CJ, *et al.* 2015. Four basic residues critical for the ion selectivity and pore blocker sensitivity of TMEM16A calcium-activated chloride channels. *Proc Natl Acad Sci U S A*. 112:3547–3552.

59 Lomize AL, Todd SC, Pogozheva ID. 2022. Spatial arrangement of proteins in planar and curved membranes by PPM 3.0. *Protein Sci*. 31:209–220.

60 Virginio C, MacKenzie A, North RA, Surprenant A. 1999. Kinetics of cell lysis, dye uptake and permeability changes in cells expressing the rat P2X7 receptor. *J Physiol*. 519:335–346.

61 Browne LE, Compan V, Bragg L, North RA. 2013. P2x7 receptor channels allow direct permeation of nanometer-sized dyes. *J Neurosci*. 33:3557–3566.

62 Mansoor SE, *et al.* 2016. X-ray structures define human P2X(3) receptor gating cycle and antagonist action. *Nature*. 538:66–71.

63 Cao L, Broomhead HE, Young MT, North RA. 2009. Polar residues in the second transmembrane domain of the rat P2X2 receptor that affect spontaneous gating, unitary conductance, and rectification. *J Neurosci*. 29:14257–14264.

64 Li M, Chang TH, Silberberg SD, Swartz KJ. 2008. Gating the pore of P2X receptor channels. *Nat Neurosci*. 11:883–887.

65 Rassendren F, Buell G, Newbolt A, North RA, Surprenant A. 1997. Identification of amino acid residues contributing to the pore of a P2X receptor. *EMBO J*. 16:3446–3454.

66 Kracun S, Chaptal V, Abramson J, Khakh BS. 2010. Gated access to the pore of a P2X receptor: structural implications for closed-open transitions. *J Biol Chem*. 285:10110–10121.

67 Liang X, Samways DSK, Cox J, Egan TM. 2019. Ca(2+) flux through splice variants of the ATP-gated ionotropic receptor P2X7 is regulated by its cytoplasmic N terminus. *J Biol Chem*. 294:12521–12533.

68 Nicke A, *et al.* 2009. A functional P2X7 splice variant with an alternative transmembrane domain 1 escapes gene inactivation in P2X7 knock-out mice. *J Biol Chem*. 284:25813–25822.

69 Samways DS, Khakh BS, Dutertre S, Egan TM. 2011. Preferential use of unobstructed lateral portals as the access route to the pore of human ATP-gated ion channels (P2X receptors). *Proc Natl Acad Sci U S A*. 108:13800–13805.

70 Pierdominici-Sottile G, Racigh V, Ormazabal A, Palma J. 2019. Charge discrimination in P2X(4) receptors occurs in two consecutive stages. *J Phys Chem B*. 123:1017–1025.

71 Racigh V, Pierdominici-Sottile G, Palma J. 2021. Ion selectivity in P2X receptors: a comparison between hP2X3 and zfP2X4. *J Phys Chem B*. 125:13385–13393.